Matter and Radiation at Extremes

RESEARCH ARTICLE | DECEMBER 30 2025

Asymmetric ion acceleration in laser-produced magnetized collisionless shocks

Tianyi Zhang ; Ao Guo; Huibo Tang ; Guangyue Hu ; Kai Huang ; Shuoting Shao; Shunyi Yang; Jiayin Xie; Gaoyuan Peng; Peng E ; Quanming Lu

Matter Radiat. Extremes 11, 027402 (2026)
https://doi.org/10.1063/5.0284676

AIP Publishing

Matter and
Radiation at Extremes

RESEARCH ARTICLE

pubs.aip.org/aip/mre

Asymmetric ion acceleration in laser-produced magnetized collisionless shocks

Cite as: Matter Radiat. Extremes 11, 027402 (2026); doi: 10.1063/5.0284676
Submitted: 9 June 2025 • Accepted: 4 December 2025 •
Published Online: 30 December 2025

Tianyi Zhang,[1] **Ao Guo,**[2] **Huibo Tang,**[1,a)] **Guangyue Hu,**[2,a)] **Kai Huang,**[1] **Shuoting Shao,**[2]
Shunyi Yang,[2] **Jiayin Xie,**[3] **Gaoyuan Peng,**[3] **Peng E,**[3] **and Quanming Lu**[2]

AFFILIATIONS

[1] School of Physics, Harbin Institute of Technology, Harbin 150001, China
[2] CAS Key Laboratory of Geospace Environment, University of Science and Technology of China, Hefei 230026, China
[3] School of Energy Science and Engineering, Harbin Institute of Technology, Harbin 150001, China

[a)] **Authors to whom correspondence should be addressed:** tanghb@hit.edu.cn and gyhu@ustc.edu.cn

ABSTRACT

Quasi-hemispherical magnetized collisionless shocks have been generated at the SG-II laser facility through the interaction between a laser-produced supersonic plasma flow and a magnetized ambient plasma, exhibiting an angular asymmetric shock profile accompanied by asymmetric ion acceleration. We have conducted test particle simulations using the electromagnetic fields derived from 2D MHD simulations to investigate the asymmetry of ion acceleration. The simulations reproduce the angular asymmetry of the shock and the ion acceleration observed in experiments. The results indicate that shock drift acceleration is the primary mechanism for ion energization in the present quasi-perpendicular magnetized shock. The asymmetric shock structure caused by nonuniform ambient plasma forms an asymmetric accelerated electric field, ultimately leading to angular asymmetric ion acceleration, which is consistent with space observations and our experimental results. Our study provides a plausible explanation for the discrepancies reported in previous ion acceleration experiments, and could contribute to understanding of the collisionless shock acceleration.

I. INTRODUCTION

Collisionless shocks are ubiquitous in the universe, prevalent in astrophysical and space physics environments. They can accelerate charged particles to extremely high energies via the diffusive shock acceleration (DSA) mechanism[1–3] and are closely linked to high-energy particle phenomena such as solar energetic particle events, anomalous cosmic rays, and galactic cosmic rays.[4–6] In DSA, particles can be accelerated to very high energy through scattering back and forth between the upstream and downstream regions of the shock, but a critical prerequisite for efficient particle acceleration via DSA is that particles must first be pre-accelerated to a specific energy threshold for injection into the acceleration process. The question of which physical process predominantly governs this pre-acceleration stage remains an unresolved key scientific challenge.[7–10]

In quasi-perpendicular shocks, two mechanisms called shock surfing acceleration (SSA)[11–13] and shock drift acceleration (SDA)[14–16] have been proposed to pre-accelerate particles. In the SSA mechanism, ions are reflected by the shock potential, bouncing between the shock front and upstream plasma and gaining energy from the inductive electric field until they enter the downstream. In the SDA mechanism, ions drift along the shock surface owing to large gradients of magnetic field, with their guiding centers moving along the inductive electric field to achieve energy gain.[17,18] Both mechanisms are influenced by shock geometry, providing key pathways for particle pre-acceleration in collisionless shock environments.

Studies of shock acceleration mechanisms in space physics have been historically constrained by limitations of undersampling and observational techniques. Gathering reproducible and comparable data for in-depth studies of the detailed structure in the evolution of magnetized shocks across the universe and the underlying particle acceleration mechanisms remains a formidable challenge. With the development of high-energy-density physics, it has become possible to generate various shock phenomena in terrestrial laboratories such as high-power laser facilities or pinch devices.[19–22] These controlled experimental environments provide high-resolution, reproducible datasets that facilitate systematic studies of fundamental processes in collisionless shocks. There have been numerous studies on electrostatic shocks and Weibel shocks in recent years, and the phenomenon of particle acceleration has also been observed.[23–28] Regarding magnetized shocks, the common approach is to generate them through interaction between the laser-ablated expanding plasma flow and the magnetized ambient plasma. Using this method, Schaeffer *et al.*[29,30] generated high-Mach-number $M_{\mathrm{ms}} \approx 12$ magnetized collisionless shocks on the LAPD device. Yao *et al.*[31,32] observed nonthermal proton spectra at the LULI laser facility, suggesting SSA as the dominant mechanism. Matsukiyo *et al.*[33] generated a developing supercritical collisionless shock in a homogeneously magnetized plasma using the Gekko XII HIPER laser facility, demonstrating key features of supercritical shocks. In our recent work at the SG-II laser facility, we have generated magnetized shocks and observed quasi-monoenergetic ion acceleration, and we have determined that SDA is the dominant mechanism.[34] However, despite several experimental studies conducted in recent years, the pre-acceleration mechanism of ions still requires further exploration in the laboratory.

In this paper, we present experimental results on asymmetric hemispherical magnetized collisionless shocks and angular asymmetric ion acceleration, and we find that the varying ion acceleration efficiencies at different spatial positions of asymmetric hemispherical shocks produce the angular asymmetric ion acceleration. Section II details the experimental setups at the SG-II laser facility, where magnetized shocks are generated via laser-driven plasma flows interacting with ambient plasma. Section III describes the setups and results of test particle simulations conducted in electromagnetic fields generated by two-dimensional magnetohydrodynamics (2D MHD), which include the shock morphology derived from MHD simulations, the acceleration mechanisms from test particle simulations, and an exploration of the factors causing acceleration asymmetry. Finally, a summary of the findings is provided in Sec. IV.

II. EXPERIMENTAL SETUP AND RESULTS

A. Experimental setup

The collisionless shock experiments were performed on the SG-II laser facility at the Shanghai Institute of Optics and Fine Mechanics (SIOM).[35,36] As shown in Fig. 1(a), two laser-irradiated CH_2 plastic planar targets were set up along the y and x directions to generate the ambient plasma and the driving piston plasma. A single coil was used to generate a magnetic field oriented along the z axis,[37] which enabled us to apply a ~6 T ambient magnetic field in the piston plasma region. The duration of the pulsed strong magnetic field was 200 ns, and thus the magnetic field could be considered to be in a steady state during the shock's evolution. The spatial distribution of the magnetic field and the shock position are shown in Fig. 1(b).

At time t_0, a precursor laser (100 J energy, 351 nm wavelength, 1 ns, $100 \times 100\ \mu\mathrm{m}^2$) ablated the left CH_2 plastic planar target to generate ambient plasma. Owing to anomalous magnetic diffusion caused by flute instabilities such as lower hybrid drift instability (LHDI) or large-Larmor-radius instability (LLRI), the ambient plasma could be fully magnetized within 12 ns.[38–40] At $t_0 + 12$ ns, the drive laser (260 J energy, 351 nm wavelength, 1 ns, $500 \times 500\ \mu\mathrm{m}^2$) ablated the upper CH_2 plastic planar target to produce a supersonic plasma flow that drove a hemispherical magnetized collisionless shock in the ambient plasma. Since the ambient plasma in our experiment was nonuniform along the x direction, as will be shown in the following, the shock formed an asymmetric hemispherical morphology, denser and more significant on the left side in Fig. 1.

B. Experimental results

Experimental results exhibit distinct features of magnetized shocks with angular asymmetric profile at $t_0 + 15$ ns. As shown in Figs. 2(a) and 2(b), schlieren imaging visualizes the contours of density gradients by deflecting probe light, while interferometry quantifies line-integrated refractive index distributions through phase shift analysis of interfering light beams.[41] A typical hemispherical shock with the typical structure of "piston," "overshoot," "ramp," and "foot" regions is revealed, and the density distribution of the laser-driven plasma during rapid expansion typically exhibits a steep exponential decay superimposed with shock structures. The plasma parameters listed in Table I satisfy the Rankine–Hugoniot (RH) relations.[42,43] The ion–ion mean free path, calculated from the experimental parameters, is ~4 mm—much larger than the shock thickness (~500 μm) and the ion Larmor radius (~800 μm). Consequently, the shock can be categorized as collisionless. Density compression also occurs without an external magnetic field, likely

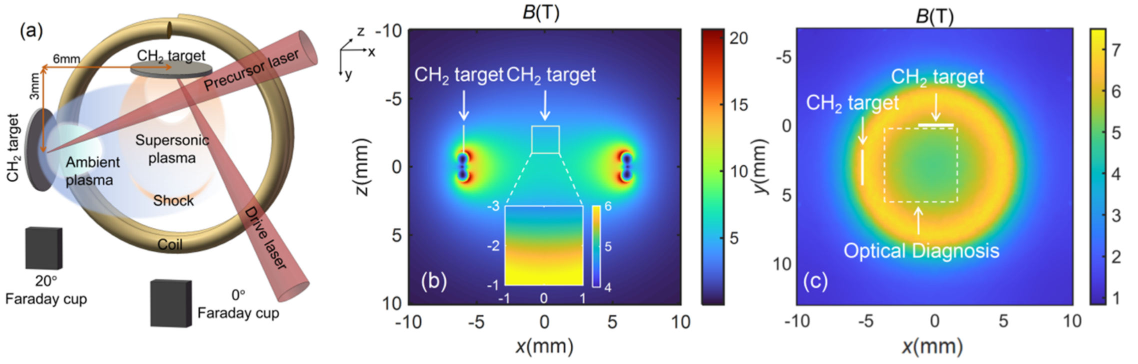

FIG. 1. (a) Experimental and diagnostic setups for magnetized shock. (b) and (c) Target positions and magnetic field structure in the *xz* and *xy* planes, respectively.

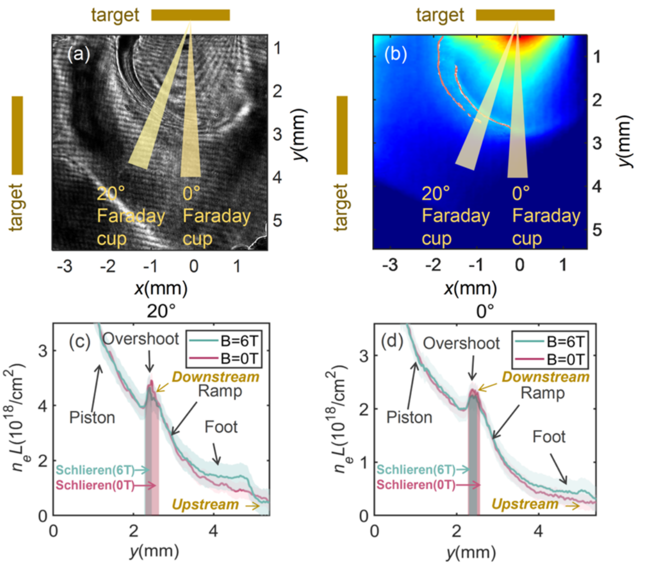

FIG. 2. (a) and (b) Optical diagnosis results of schlieren imaging [(a) and red line in (b)] and interferometry (b) at $t_0 + 15$ ns. (c) and (d) Line-integrated density profiles measured in the presence and absence of magnetic fields at 0° and 20°, respectively, with the fringes given by schlieren imaging around the shock (vertical shaded region).

TABLE I. Parameters of magnetized shock.[a]

Parameter	Experimental value
Shock velocity V	400–500 km/s
Magnetic field strength B	5–6 T
Electron temperature T_e	40 ± 10 eV
Upstream shock density n_1	1.5×10^{18} cm^{-3}
Downstream shock density n_2	5×10^{18} cm^{-3}
Plasma beta β	0.9–1.4
Alfvén Mach number M_A	7–11
Compression ratio r	3.5–3.8

[a] The shock velocity V was derived from fitting the shock front tracked via optical measurements at different times. The electron temperature T_e was estimated from Thomson scattering measurements (and may be an overestimate because of electron heating by the probe laser) in other experiments, where the laser and target parameters were similar to ours. The upstream and downstream electron densities n_1 and n_2 were estimated from Abel inversion of interferometric data. The Alfvén Mach number $M_A = v/v_A$ is defined as the ratio of the flow velocity v to the Alfvén velocity $v_A = B/(\mu_0 n_i m_i)^{1/2}$, where B is the magnetic field strength, μ_0 is the vacuum permeability, n_i is the number density of the plasma, and m_i is the ion mass (analogously to the ordinary sonic Mach number $M = v/c_s$, defined as the ratio of the flow velocity v to the sound velocity c_s).

owing to a self-generated magnetic field (~1 T, generated by the Biermann battery effect) during shock generation as mentioned in previous studies.[44] The magnetic field provides extra compression, making the overshoot narrower. Additionally, the proportion of reflected ions is much higher in the presence of an external magnetic field, which forms the distinct foot structure. These two features highlight significant differences between magnetized and nonmagnetized cases. Meanwhile, the shock displays angular asymmetric characteristics, which are denser and wider on the left, and the compressive effect of the external magnetic field on the schlieren band is also more obvious.

The ion velocity spectra obtained from the experiments also exhibit angular asymmetric characteristics, which are measured by Faraday cups positioned at angles of 0° and 20° relative to the piston target's normal direction, located 18 and 23 cm, respectively, from the target center. The Faraday cup converts ion current into velocity distribution using the time-of-flight method, enabling the identification of the piston plasma and ions accelerated by the shock, while signals generated by the low-velocity background plasma are negligible. As shown in Fig. 3, the data from the Faraday cup directly below the target (0°, 18 cm) exhibit an obvious double-peak distribution in the velocity spectrum. The lower-speed peak (~500 km/s) corresponds to the piston plasma, and the higher-speed peak represents the accelerated fast ions, around 1200 km/s. Similar fast ion peak components have been detected in many observations of Earth's bow shock.[45,46]

By contrast, the data from the Faraday cup positioned obliquely below (20°, 23 cm) show only a single-peak structure, indicating significantly weaker ion acceleration. Weaker ion acceleration correlates with a denser shock, which indicates that the shock

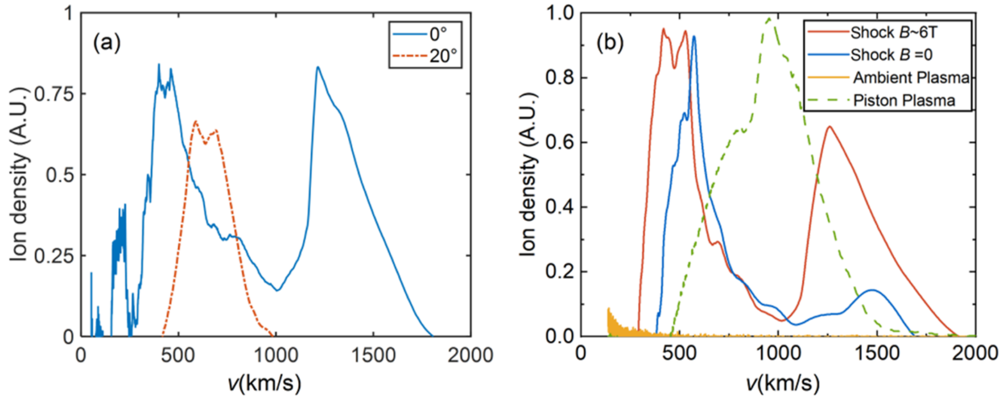

FIG. 3. (a) Ion velocity spectra measured by Faraday cups positioned at 0° (directly below) and 20° (obliquely below) view angles with respect to the normal direction of the piston target, with an external magnetic field $B \sim 6$ T. (b) Ion velocity spectra at 0° for $B = 6$ T, $B = 0$ T, piston plasma only, and ambient plasma only.

characteristics may alter the ion acceleration efficiency. A similar phenomenon has been observed in corotating interaction region (CIR) shocks within space environments.[47] Observations from the MMS and WIND satellites indicate that the enhancement of the convective drift electric field has a dominant effect on the particle acceleration efficiency in collisionless shocks. Specifically, even as the shock speed decreases, along with reductions in compression ratio and thinning of shock thickness, the strengthening of this electric field significantly boosts particle acceleration.

We also conducted comparative experiments under other conditions to verify the acceleration of ions by the magnetized shock. As shown in Fig. 3(b), when only the piston plasma is present, the velocity spectrum exhibits a single peak near 1000 km/s. When only ambient plasma is present, the Faraday cup at 0° detects almost no ions. A very small number of ions are accelerated by the shock in the absence of an external magnetic field. Significant ion acceleration occurs only when both ambient plasma and an external magnetic field (5–6 T) are simultaneously present, indicating a pronounced shock acceleration process.

III. SIMULATION SETUP AND RESULTS

To investigate the causes of asymmetric ion acceleration in the shock, we conducted numerical simulations. In our previous study, 1D particle-in-cell (PIC) simulations were conducted.[27,48] The results of those simulations showed that shock-reflected ions are accelerated through two different mechanisms: shock drift acceleration (SDA) and shock surfing acceleration (SSA), with SDA being the primary process. Very few ions undergo double reflection by the shock, achieving higher velocities. However, 1D simulations fail to capture the 2D asymmetric characteristics of quasi-hemispherical shocks, while 2D PIC simulations incur enormous computational cost. Therefore, for the present exploration, we employed a test particle method using the electromagnetic field background obtained from 2D MHD simulations.

A. Setup for test particle simulations using 2D MHD-generated electromagnetic fields

In our experiments, the collisionless shocks driven by the laser plasma were typically quasi-hemispherical. However, owing to the nonuniform distribution of ambient plasma density along the x direction, the magnetized shock exhibited an asymmetric profile. To reproduce the shock features observed in the experiments, we first employed 2D MHD simulations to replicate the shock characteristics and obtain the electromagnetic field evolution. Subsequently, test particle simulations were conducted using the electromagnetic field background from the MHD simulations to investigate the relationship between the asymmetric characteristics of the shock profile and ion acceleration efficiency.

2D MHD simulations were performed using the FLASH code, which includes nonideal effects such as artificial viscosity and resistivity, amplifying collisional effects to compensate for dissipation from ion reflection, and promoting the formation of a magnetized shock.[49,50] The primary purpose of using MHD was to simulate the large-scale interaction between the laser-driven plasma piston and the magnetized ambient plasma, thereby providing electromagnetic field structures for subsequent test particle simulation. The ambient density measured by optical interferometry exhibits an exponential distribution along the x direction, and we used the density distribution from the precursor laser only experiment as the initial condition for the MHD simulation. The simulation region was 1.6×1.6 cm^2 and filled with low-temperature plasma. The main-pulse laser intensity was 1.2×10^{12} W/cm^2, with a focal spot radius of 100 μm and a duration of 1 ns. For the MHD simulation, a perpendicular 7 T magnetic field was applied in the simulation plane.

The density, pressure, and velocity at various times output by the MHD simulation were used to obtain the electromagnetic field information, which served as the electromagnetic field background for the test particles. The test particle method is a common method for studying ion acceleration. The equation of motion of ions in a given electromagnetic field is

$$\frac{d\boldsymbol{v}}{dt} = \frac{q}{m}(\boldsymbol{E} + \boldsymbol{v} \times \boldsymbol{B}),$$

where $\boldsymbol{v}$, q, and m are the velocity, charge, and mass of the proton, t is time, and $\boldsymbol{E}$ and $\boldsymbol{B}$ are the electric and magnetic fields at the position of the ion. In our test particle code, the equations of motion for charged particles in electromagnetic field were integrated using the Boris algorithm. The electric and magnetic fields were obtained from 2D MHD simulation and output to a 2D grid with a resolution of 7.8 μm ($\sim r_{ci}/100$, where r_{ci} is the ion gyroradius; for the given simulation parameters, r_{ci} is about 0.7–2.5 mm). Test particles were randomly placed into these grids, with their velocities randomized to follow a Maxwellian distribution. Coupling between particles and fields was achieved through nearest-neighbor interpolation of field values at particle positions. The time step of the simulation was set to 0.001 ns, and the total calculation time was 2.5 ns. The electromagnetic field information was input and updated every 0.1 ns. This ensured that the simulation could accurately capture the dynamic changes of the electromagnetic field during the ion motion process.

B. Shock obtained from MHD simulations

The plasma density at 3 ns from MHD simulation is shown in Fig. 4, which demonstrates that a collisionless shock is formed by the impact of a plasma piston in the magnetized ambient plasma. As shown in Fig. 4(a), the simulated region exhibits an exponential ambient density distribution along the x direction, with higher density on the left side, resulting in earlier shock formation in this area. Overall, the shock presents an asymmetric quasi-hemispherical shape, and the magnetic field is stronger in the high-density region. The simulation results show that the shock propagates with a velocity of about 600 km/s with Alfvén Mach number M_A about 4–6. The temperature of the piston plasma is ~200–300 eV, and the electron density is about 10^{19} cm^{-3}. We also find that the shock compression ratio is greater than 3. All these parameters are consistent with experimental results.[34] The longitudinal density distribution reveals typical shock overshoot and ramp structures, with a lack of a foot structure. It should be noted that ion reflection does not provide dissipation for collisionless shocks in MHD simulations; instead, dissipation occurs through other nonideal effects.

C. Acceleration of test particles

The results for test particles exhibit angular asymmetric features. Figure 5(a) shows the spatial distribution of test particles, where each dot represents a test ion, and the color indicates the

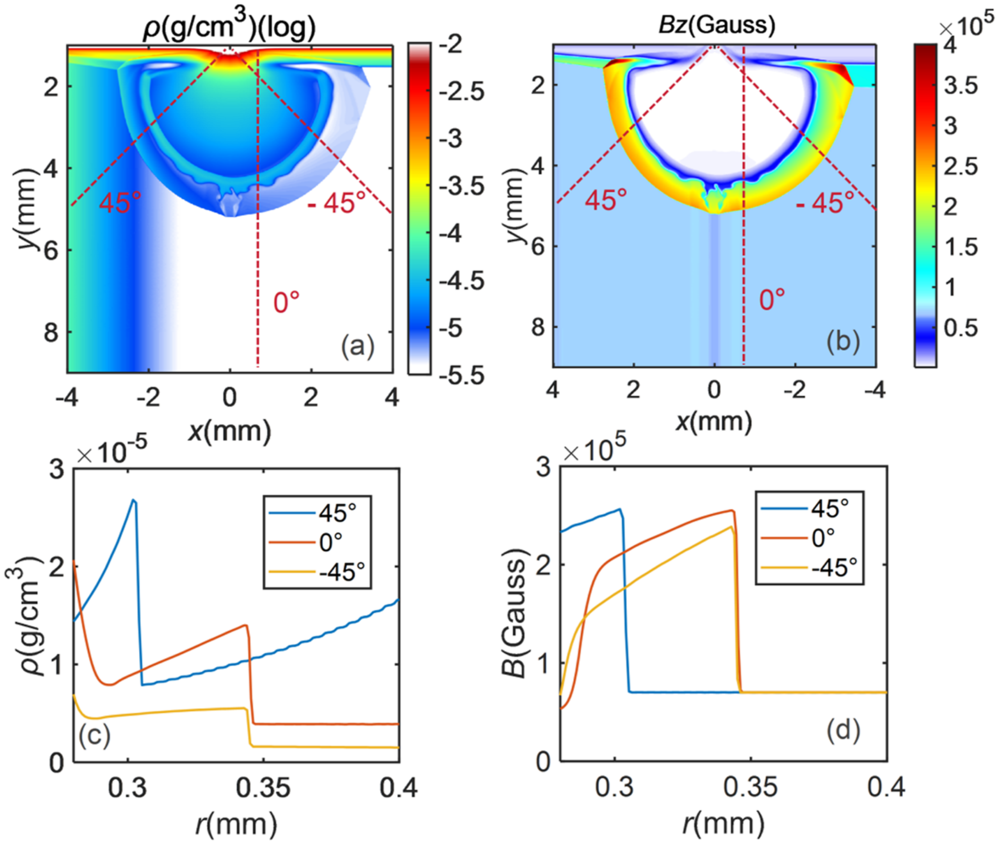

FIG. 4. Shock profiles obtained by MHD simulation: (a) mass density; (b) magnetic field; (c) and (d) Profiles of density and magnetic field, respectively, along the red dashed lines in Figs. 4(a) and 4(b).

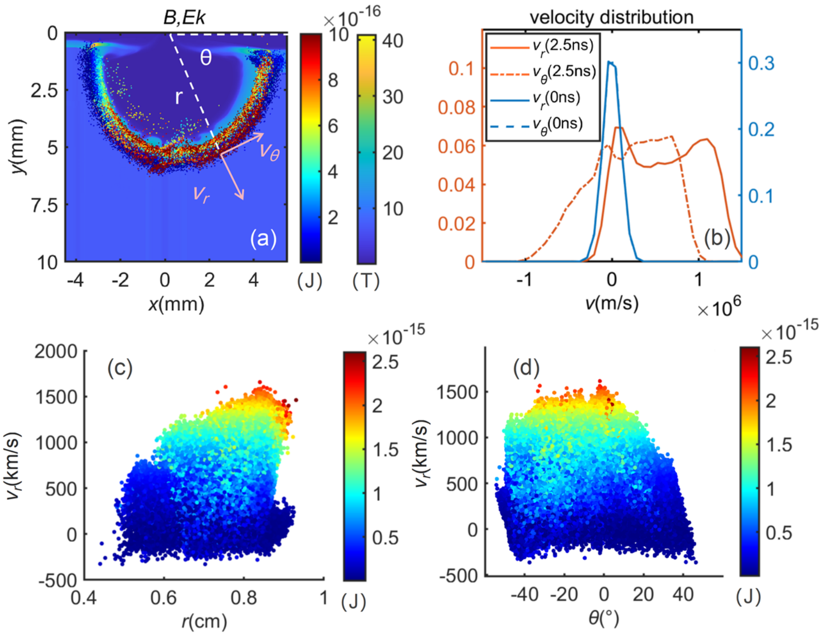

FIG. 5. Test particle simulation results. (a) Test ion positions and energies at 2.5 ns. The color of each particle represents its energy, v_r is the radial velocity, and v_θ is the angular velocity. (b) Initial (blue line) and accelerated (red line) velocity-distribution spectra. After shock acceleration, an acceleration peak appears in the spectral profile. (c) and (d) Particle phase-space distributions in the r–v and θ–v planes, respectively.

particle energy. The test ions are accelerated near the spherical shock front, with the acceleration effect depending on position. Figures 5(b)–5(d) depict the velocity spectra and phase-space distributions in different directions. Here, v_r is the radial velocity component in polar coordinates with the laser incidence point as the origin, and v_θ is the angular velocity component. Figure 5(b) reveals that as the shock propagates in the r direction, both v_r and v_θ experience significant acceleration. The velocity distribution of test ions transitions from an initial single-peak to a double-peak structure, indicating that a portion of the ions are accelerated. This result is consistent with the experimental results (Fig. 3) and 1D PIC simulations. The agreement between simulation and experiment is primarily reflected in the high-velocity peak, which is separated from the piston peak, reaches up to approximately three times the shock speed (1500 km/s), and exhibits clear angular asymmetry. Figure 5(c) demonstrates that in the region at larger r positions, some ions reach higher energies, indicating that these particles experience an acceleration process near the shock front and then move into the upstream region. Figure 5(d) shows the characteristics of the angular distribution of test particles. From the direction perpendicular to the laser (−90° and 90°) to the direction parallel to the laser (0°), the velocity of accelerated fast ions gradually increases. At the same time, the acceleration on both sides of the spherical surface exhibits asymmetry. It is stronger on the right side, where the background density is lower and the shock forms later compared with the other side. Some extra higher-energy ions are predominantly located at the 0° position, which may be caused by potential numerical instabilities at the laser-incidence grids. In the FLASH code, numerical errors occur when the laser is normally incident on the target surface, and oblique incidence of the laser can eliminate laser channel interference.

Through force analysis of the particles, we conclude that the dominant acceleration mechanism is SDA. In Fig. 6(a), we illustrate the velocities and force conditions for two typical accelerated particles. In the shaded regions, the two particles undergo respective acceleration processes. During this period, the F_{mag} ($=qvB$) dominates over F_{ele} ($=qE$), which supports the conclusion that ion acceleration is primarily driven by SDA. We performed a statistical analysis of the contributions of magnetic and electric forces during the acceleration of all particles (the dot product of the force and the displacement of the particle during its interaction with the shock). As shown in Fig. 6(b), the majority of reflected ions are dominated by magnetic work, and the vast majority of accelerated particles are concentrated in the SDA region, which also agrees with our PIC simulation results.[48] Additionally, variations in the plasma β value may lead to differences in the dominant acceleration mechanisms. Higher β enhances the electrostatic potential, inducing additional ion reflection. This may explain why SSA is considered to be the primary pre-acceleration mechanism in some high-β studies.

D. Effect of shock asymmetry on ion acceleration

We statistically analyzed particle acceleration at three typical angles and confirmed its angular dependence. Initial test particles were distributed upstream of the entire hemispherical shock, with acceleration occurring at all angular positions, but varying by location. To quantify these differences, we focused on three specific angles relative to the polar axis, placing particles in small fan-shaped regions (−45° ± 2.5°, 0 ° ± 2.5°, and 45 ° ± 2.5° in Fig. 4) at simulation onset and tracking their shock-driven acceleration. Figures 7(a)–7(c) show the total kinetic energy spectrum, the kinetic energy spectrum along the r direction, and the kinetic energy spectrum perpendicular to the r direction, respectively, and Figs. 7(d)–7(f) show the total velocity spectrum, the velocity spectrum along the r direction, and the velocity spectrum perpendicular to the r direction, respectively. Regardless of the type of distribution analyzed, the acceleration peak becomes more obvious and the velocities of the accelerated particles increase in the region with negative angles. In particular, the velocity in the r direction is significantly influenced by angle, which is consistent with the experimental results in Fig. 2. It is worth noting that Fig. 7 displays the velocity peak of the ambient plasma, while Fig. 2 includes all ions detected by the Faraday cups, which incorporates a portion of the piston plasma. In our experiments, the Faraday cup positioned at 0° measured a double-peak distribution,

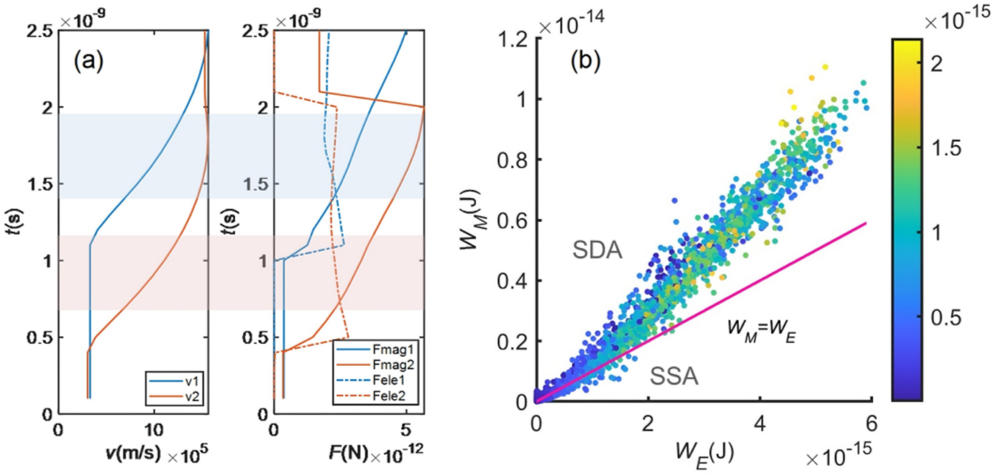

FIG. 6. (a) Velocities and forces for two typical test particles at 2.5 ns. (b) Statistical results for test ions.

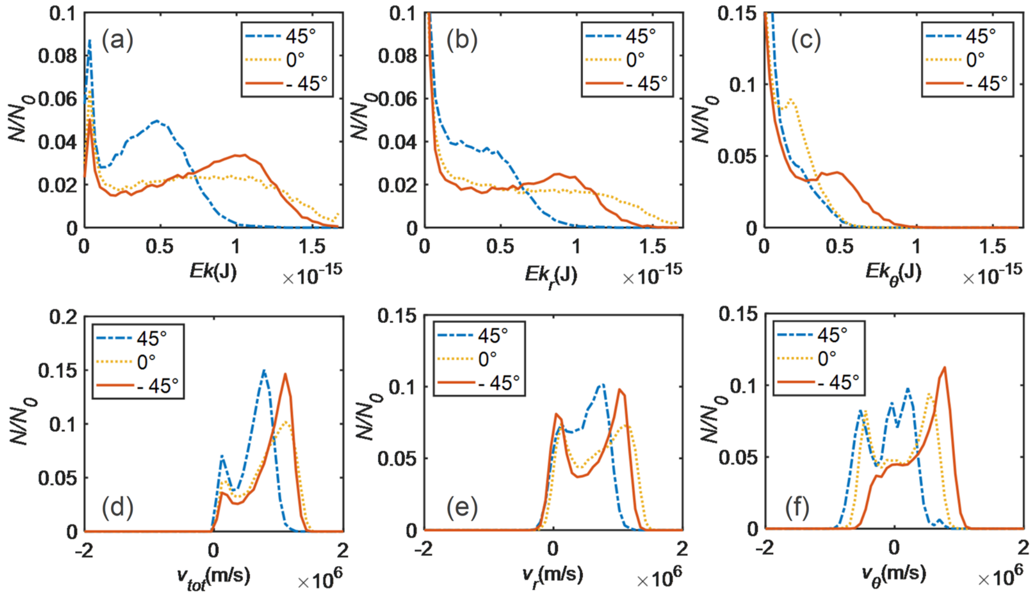

FIG. 7. Energy spectra and velocity distributions at different angles: (a) and (d) Total energy and total velocity; (b) and (e) radial energy and radial velocity; (c) and (f) angular energy and angular velocity.

while this is less obvious for the Faraday cup positioned obliquely below (20°), owing to overlap between the high-energy peak (700 km/s) and the piston peak (500 km/s), and an obvious accelerated quasi-single-energy spectrum cannot be observed.

In the test particle simulation, most of the accelerated ions were found to experience SDA, with the motional electric field $\boldsymbol{v} \times \boldsymbol{B}$ playing a predominant role. As shown in Fig. 8(a), the electric field is primarily composed of the angular component E_θ. Averaging this

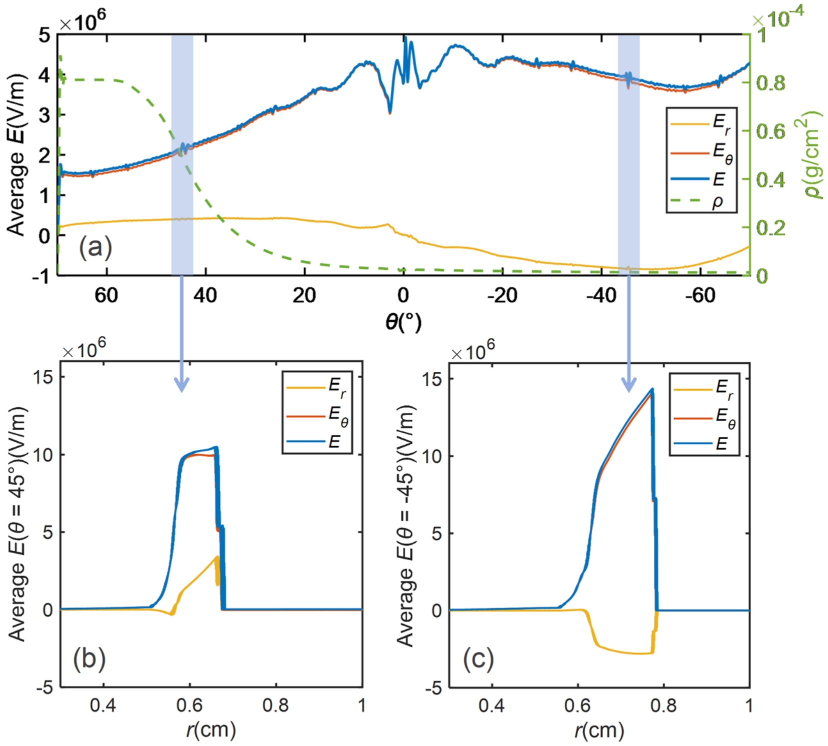

FIG. 8. Magnitude of electric field (motional electric field) and density at different θ and r positions. (a) Average electric field components (calculated over the shock thickness) and density at various values of θ. (b) and (c) Distribution of electric field along the shock normal direction at θ = 45° and −45°, respectively.

over the shock thickness range gives $E_{\text{ave}} = \int_0^r E_\theta dr / \int_0^r dr$, which also exhibits angular asymmetry, and this electric field strength increases as the background density decreases. As can be seen in Figs. 8(b) and 8(c), the magnitude of the electric field at 45° is smaller than that at −45°, resulting in a weaker acceleration effect. This asymmetry originates from the inhomogeneous distribution of the ambient density, which causes inconsistent magnitudes of the electric field at the shock front and thus affects the ion acceleration efficiency. In addition to the electric field magnitude, the pressure gradient may also influence ion acceleration. We analyzed the magnetic field profile and compression ratios, which indicated little variation across all regions within the spherical shock, suggesting that the acceleration efficiency primarily hinges on the magnitude of the electric field. The simulation results are consistent with our previous experimental results.[34] The correlation between this acceleration and the electric field is also reflected in observations by the Magnetospheric Multiscale (MMS) mission,[47] which studied the evolution of the in situ acceleration of solar wind suprathermal electrons in two corotating interaction regions (CIRs) observed by WIND and MMS 1 at 1 AU in January 2018 and February 2020, respectively. The results show that the acceleration efficiency of solar wind suprathermal electrons increases with the strength of the convective electric field E_{drift}.

IV. CONCLUSIONS

It has been found that magnetized shocks produce significantly greater ion acceleration than those without an external magnetic field, and we have demonstrated the asymmetric characteristics of quasi-hemispherical magnetized collisionless shocks and their associated ion acceleration. Test particle simulations, using the electromagnetic field background generated by 2D MHD simulation, reproduce the experimental asymmetries of the quasi-perpendicular shock structure and the proton spectra. We have identified shock drift acceleration (SDA) as the dominant ion acceleration mechanism. We have further found that the motional electric field strength significantly affects ion acceleration efficiency. Specifically, a stronger motional electric field enhances the acceleration efficiency, and therefore asymmetric shocks produces angular asymmetric ion acceleration. These findings are consistent with experimental results and the observations of the Earth's foreshock region by the MMS mission. This work offers a potential explanation for the varying results reported in previous studies on ion acceleration, highlighting the importance of shock geometry and electric field in collisionless shock environments, thus providing a more comprehensive understanding of the underlying acceleration dynamics.

While MHD simulations effectively capture large-scale plasma dynamics and electromagnetic field structures, they do not inherently resolve kinetic-scale dissipation mechanisms, such as ion reflection and wave–particle interactions. By contrast, PIC simulations self-consistently incorporate kinetic effects, enabling the representation of nonequilibrium features, including a defined shock foot and reflected ion populations. Nonetheless, both our test particle simulations using 2D MHD-generated electromagnetic fields and our earlier 1D PIC results consistently demonstrate that SDA serves as the dominant ion acceleration mechanism. This suggests that the large-scale electromagnetic field structures essential to SDA are accurately reproduced within the MHD framework.

ACKNOWLEDGMENTS

This work is supported by the National Natural Science Foundation of China (Grant Nos. 12205298 and 12175230), the Natural Science Foundation of Heilongjiang Province of China (Grant No. LH2024A010), the Fundamental Research Funds for the Central Universities, Controversial and Disruptive Projects of the Chinese Academy of Sciences (Grant No. FGSDFX-0001), and the USTC Research Funds of the Double First-Class Initiative (Grant No. YD2140002006). We would like to thank the staff of the Shenguang II laser facility at the Shanghai Institute of Optics and Fine Mechanics, Chinese Academy of Sciences, for their assistance in conducting these experiments. The software used in this work was developed in part by the DOE NNSA- and DOE Office of Science-supported Flash Center for Computational Science at the University of Chicago and the University of Rochester.

AUTHOR DECLARATIONS

Conflict of Interest

The authors have no conflicts to disclose.

Author Contributions

Tianyi Zhang: Data curation (equal); Methodology (equal); Writing – original draft (equal). **Ao Guo**: Data curation (equal); Methodology (equal). **Huibo Tang**: Funding acquisition (equal); Methodology (equal); Writing – review & editing (equal). **Guangyue Hu**: Funding acquisition (equal); Methodology (equal); Writing – review & editing (equal). **Kai Huang**: Software (equal). **Shuoting Shao**: Data curation (equal). **Shunyi Yang**: Methodology (equal); Software (equal). **Jiayin Xie**: Visualization (equal). **Gaoyuan Peng**: Visualization (equal). **Peng E**: Funding acquisition (equal); Supervision (equal). **Quanming Lu**: Funding acquisition (equal); Investigation (equal); Supervision (equal).

DATA AVAILABILITY

The data that support the findings of this study are available from the corresponding author upon reasonable request.

REFERENCES

[1] E. Fermi, "On the origin of the cosmic radiation," Phys. Rev. **75**, 1169–1174 (1949).

[2] A. R. Bell, "The acceleration of cosmic rays in shock fronts - I," Mon. Not. Roy. Astron. Soc. **182**, 147–156 (1978).

[3] G. F. Krymskii, "A regular mechanism for accelerating charged particles at the shock front," Dokl. Akad. Nauk SSSR **234**, 1306–1308 (1977).

[4] R. D. Blandford and J. P. Ostriker, "Particle acceleration by astrophysical shocks," Astrophys. J. **221**, L29–L32 (1978).

[5] G. Li, G. P. Zank, and W. K. M. Rice, "Energetic particle acceleration and transport at coronal mass ejection–driven shocks," J. Geophys. Res. **108**(A2), 1082–1101, https://doi.org/10.1029/2002JA009666 (2003).

[6] G. P. Zank, G. Li, V. Florinski, Q. Hu, D. Lario *et al.*, "Particle acceleration at perpendicular shock waves: Model and observations," J. Geophys. Res.: Space Phys. **111**, A06108, https://doi.org/10.1029/2005ja011524 (2006).

[7] B. Lembège, J. Giacalone, M. Scholer, T. Hada, M. Hoshino *et al.*, "Selected problems in collisionless-shock physics," Space Sci. Rev. **110**, 161–226 (2004).

[8] A. Balogh and R. A. Treumann, *Physics of Collisionless Shocks* (Springer Science+Business Media, New York, 2013), pp. 405–500.

[9] J. Park, D. Caprioli, and A. Spitkovsky, "Simultaneous acceleration of protons and electrons at nonrelativistic quasiparallel collisionless shocks," Phys. Rev. Lett. **114**, 085003 (2015).

[10] M. Shalaby, R. Lemmerz, T. Thomas, and C. Pfrommer, "The mechanism of efficient electron acceleration at parallel nonrelativistic shocks," Astrophys. J. **932**, 86 (2022).

[11] R. Z. Sagdeev, "Cooperative phenomena and shock waves in collisionless plasmas," Rev. Plasma Phys. (USSR) **4**, 23–91 (1966).

[12] M. A. Lee, V. D. Shapiro, and R. Z. Sagdeev, "Pickup ion energization by shock surfing," J. Geophys. Res.: Space Phys. **101**, 4777–4789, https://doi.org/10.1029/95ja03570 (1996).

[13] V. D. Shapiro and D. Üçer, "Shock surfing acceleration," Planet. Space Sci. **51**, 665–680 (2003).

[14] M. C. Begelman and J. G. Kirk, "Shock-drift particle acceleration in superluminal shocks: A model for hot spots in extragalactic radio sources," Astrophys. J. **353**, 66–80 (1990).

[15] T. P. Armstrong, M. E. Pesses, and R. B. Decker, *Shock Drift Acceleration*, Geophysical Monograph Series (American Geophysical Union, 1985), Vol. 35, pp. 271–285.

[16] R. Decker, "Computer modeling of test particle acceleration at oblique shocks," Space Sci. Rev. **48**, 195–262 (1988).

[17] F. Guo and J. Giacalone, "The acceleration of thermal protons at parallel collisionless shocks: Three-dimensional hybrid simulations," Astrophys. J. **773**, 158 (2013).

[18] Z. Yang, Q. Lu, B. Lembège, and S. Wang, "Shock front nonstationarity and ion acceleration in supercritical perpendicular shocks," J. Geophys. Res. **114**, A03111, https://doi.org/10.1029/2008JA013785 (2009).

[19] Y. Kuramitsu, Y. Sakawa, T. Morita, C. D. Gregory, J. N. Waugh *et al.*, "Time evolution of collisionless shock in counterstreaming laser-produced plasmas," Phys. Rev. Lett. **106**, 175002 (2011).

[20] J. S. Ross, D. P. Higginson, D. Ryutov, F. Fiuza, R. Hatarik *et al.*, "Transition from collisional to collisionless regimes in interpenetrating plasma flows on the national ignition facility," Phys. Rev. Lett. **118**, 185003 (2017).

[21] N. L. Kugland, D. D. Ryutov, P.-Y. Chang, R. P. Drake, G. Fiksel *et al.*, "Self-organized electromagnetic field structures in laser-produced counter-streaming plasmas," Nat. Phys. **8**, 809–812 (2012).

[22] W. Fox, G. Fiksel, A. Bhattacharjee, P. Y. Chang, K. Germaschewski *et al.*, "Filamentation instability of counterstreaming laser-driven plasmas," Phys. Rev. Lett. **111**, 225002 (2013).

[23] C. M. Huntington, F. Fiuza, J. S. Ross, A. B. Zylstra, R. P. Drake *et al.*, "Observation of magnetic field generation via the Weibel instability in interpenetrating plasma flows," Nat. Phys. **11**, 173–176 (2015).

[24] D. Yuan, Y. Li, M. Liu, J. Zhong, B. Zhu *et al.*, "Formation and evolution of a pair of collisionless shocks in counter-streaming flows," Sci. Rep. **7**, 42915 (2017).

[25] H. He, B. Qiao, X. F. Shen, W. P. Yao, Y. Xie *et al.*, "High-flux high-energy ion beam production from stable collisionless shock acceleration by intense petawatt-picosecond laser pulses," New J. Phys. **21**, 033035 (2019).

[26] J. L. Jiao, S. K. He, H. B. Zhuo, B. Qiao, M. Y. Yu *et al.*, "Experimental observation of ion–ion acoustic instability associated with collisionless shocks in laser-produced plasmas," Astrophys. J., Lett. **883**, L37 (2019).

[27] C. K. Li, V. T. Tikhonchuk, Q. Moreno, H. Sio, E. D'Humières *et al.*, "Collisionless shocks driven by supersonic plasma flows with self-generated magnetic fields," Phys. Rev. Lett. **123**, 055002 (2019).

[28] D. Yuan, Z. Lei, H. Wei, Z. Zhang, J. Zhong *et al.*, "Electron stochastic acceleration in laboratory-produced kinetic turbulent plasmas," Nat. Commun. **15**, 5897 (2024).

[29] D. B. Schaeffer, W. Fox, D. Haberberger, G. Fiksel, A. Bhattacharjee *et al.*, "Generation and evolution of high-mach-number laser-driven magnetized collisionless shocks in the laboratory," Phys. Rev. Lett. **119**, 025001 (2017).

[30] D. B. Schaeffer, W. Fox, D. Haberberger, G. Fiksel, A. Bhattacharjee *et al.*, "High-Mach number, laser-driven magnetized collisionless shocks," Phys. Plasmas **24**, 122702 (2017).

[31] W. Yao, A. Fazzini, S. N. Chen, K. Burdonov, P. Antici *et al.*, "Detailed characterization of a laboratory magnetized supercritical collisionless shock and of the associated proton energization," Matter Radiat. Extremes **7**, 014402 (2021).

[32] W. Yao, A. Fazzini, S. N. Chen, K. Burdonov, P. Antici *et al.*, "Laboratory evidence for proton energization by collisionless shock surfing," Nat. Phys. **17**, 1177–1182 (2021).

[33] S. Matsukiyo, R. Yamazaki, T. Morita, K. Tomita, Y. Kuramitsu *et al.*, "High-power laser experiment on developing supercritical shock propagating in homogeneously magnetized plasma of ambient gas origin," Phys. Rev. E **106**, 025205 (2022).

[34] H. B. Tang, Y. F. Hao, G. Y. Hu, Q. M. Lu, C. Ren *et al.*, "Laboratory observation of ion drift acceleration via reflection off laser-produced magnetized collisionless shocks," Sci. Adv. **11**, eadn3320 (2025).

[35] P. Hu, G.-y. Hu, Y.-l. Wang, H.-b. Tang, Z.-c. Zhang *et al.*, "Pulsed magnetic field device for laser plasma experiments at Shenguang-II laser facility," Rev. Sci. Instrum. **91**, 014703 (2020).

[36] H.-c. Si, H.-b. Tang, W. Liu, P. Yuan, and G.-y. Hu, "Digital holographic interferometry for diagnosing the density profile of laser-produced collisionless shock," Rev. Sci. Instrum. **94**, 083505 (2023).

[37] Y. L. Wang, G. Y. Hu, P. Hu, H. B. Tang, P. Yuan *et al.*, "Compact pulsed intense magnetic field generator for Shenguang-II upgrade laser facility," J. Instrum. **14**, P09024 (2019).

[38] N. Brenning, R. L. Merlino, D. Lundin, M. A. Raadu, and U. Helmersson, "Faster-than-Bohm cross-*B* electron transport in strongly pulsed plasmas," Phys. Rev. Lett. **103**, 225003 (2009).

[39] C. Niemann, W. Gekelman, C. G. Constantin, E. T. Everson, D. B. Schaeffer *et al.*, "Dynamics of exploding plasmas in a large magnetized plasma," Phys. Plasmas **20**, 012108 (2013).

[40] D. B. Schaeffer, E. T. Everson, D. Winske, C. G. Constantin, A. S. Bondarenko *et al.*, "Generation of magnetized collisionless shocks by a novel, laser-driven magnetic piston," Phys. Plasmas **19**, 070702 (2012).

[41] W. Wei, X. Li, J. Wu *et al.*, "Interferometric and schlieren characterization of the plasmas and shock wave dynamics during laser-triggered discharge in atmospheric air," Phys. Plasmas **21**(8), 083112 (2014).

[42] D. A. Tidman, N. A. Krall, and M. Dryer, "Shock waves in collisionless plasmas," Am. J. Phys. **40**, 1055 (1972).

[43] D. B. Schaeffer, E. T. Everson, A. S. Bondarenko, S. E. Clark, C. G. Constantin *et al.*, "Laser-driven, magnetized quasi-perpendicular collisionless shocks on the large plasma device," Phys. Plasmas **21**, 056312 (2014).

[44] D. B. Schaeffer, W. Fox, R. K. Follett, G. Fiksel, C. K. Li *et al.*, "Direct observations of particle dynamics in magnetized collisionless shock precursors in laser-produced plasmas," Phys. Rev. Lett. **122**, 245001 (2019).

[45] H. Madanian, S. J. Schwartz, S. A. Fuselier, D. Burgess, D. L. Turner *et al.*, "Direct evidence for magnetic reflection of heavy ions from high Mach number collisionless shocks," Astrophys. J., Lett. **915**, L19 (2021).

[46] J. M. Broll, S. A. Fuselier, K. J. Trattner, S. J. Schwartz, J. L. Burch *et al.*, "MMS observation of shock-reflected He^{++} at Earth's quasi-perpendicular bow shock," Geophys. Res. Lett. **45**, 49–55, https://doi.org/10.1002/2017gl075411 (2018).

[47] X. N. Guo, L. H. Wang, W. Y. Li, Q. Y. Ma, L. Yang *et al.*, "Evolution of electron acceleration by corotating interaction region shocks at 1 au," Astrophys. J. **966**, L12 (2024).

[48] A. Guo, H. Tang, J. Ren, G. Hu, and S. Lu, "Ion dynamics in laser-produced collisionless perpendicular shock: One-dimensional particle-in-cell simulation," Plasma Sci. Technol. **25**, 065301 (2023).

[49] B. Fryxell, K. Olson, P. Ricker, F. X. Timmes, M. Zingale *et al.*, "FLASH: An adaptive mesh hydrodynamics code for modeling astrophysical thermonuclear flashes," Astrophys. J., Suppl. Ser. **131**, 273 (2000).

[50] A. J. Kemp and J. Meyer-ter-Vehn, "An equation of state code for hot dense matter, based on the QEOS description," Nucl. Instrum. Methods Phys. Res., Sect. A **415**, 674–676 (1998).